

Enhancing the Thermal Dissipation in Batteries via Inclusion of Central Heat Sink

Asghar Aryanfar^{*†}, Fadi Elias[‡], William A. Goddard III [§]

[†] *Bogazici University, Bebek, Istanbul, Turkey 34342*

[‡] *American University of Beirut, Riad El-Solh, Beirut, Lebanon 1107 2020*

[§] *California Institute of Technology, 1200 E California Blvd, Pasadena, CA, USA 91125*

©Accepted for Publication in **J Electrochemical Energy Storage and Conversion** ©

Abstract

The generation of heat within the rechargeable batteries during the charge-discharge cycles is inevitable, making the heat dissipation a very critical part of their design and operation procedure, as a safety and sustainability measure. In particular, when heat gets the least possibility to escape from the electrode surface, the boundary of the packaging material remains the sole heat dissipator. In this regard, the heat gets accumulated in the central zone, making it the most critical, since it has the least possibility to escape to the surroundings. Anticipating such a heat trap, a central heat sink component is devised, where the role of its conductivity and the relative scale is analyzed based on the formation of transient and steady state temperature profiles. Additionally, an analytical solution is attained for the location of the maximum temperature, where its value and correlation with the electrolyte conductivity, heat generation rate and scale of the cell has been quantified. Due to the existence of the curved boundaries, it is shown that the time versus space resolution for capturing the transient evolution of the temperature is more strict than the flat surface and analytically acquired as $\approx 33\%$ smaller value. Such enhanced design and subsequent analysis is critical for planning sustainable and cost effective packaging to avoid the ignition and failure of the respective electrolyte.

Keywords: Heat dissipation, Design, Batteries, Thermal management.

1 Introduction

Everyday technology is tending to moderate itself at exponential rates [1]. While energy-sourcing from traditional fossil fuels has proven not to be environmentally friendly, the new electric powered age has

^{*}Corresponding author, Email: aryanfar@caltech.edu

been initiated during the recent decades. Furthermore, with increasing involvement of silicon-based portables in daily life, the demand for electric power has become very critical. In order to meet this call, it is imperative to equip the electric power sources with the greatest amount of energy density, which could get utilized over an extensive period [2, 3]. Rechargeable lithium-based battery is a clean and dense source of electric energy in this regard, which operates fundamentally via chemical reactions to generate electric current and can get scaled-up to acceptable sizes and designs for optimal comfort in electronics and transportation [4, 5].

However, the chemical reaction is exothermic, meaning that energy is released in the process, which heats up the battery and if not dissipated systematically, it leads to the thermal runaway in the electrolyte, causing safety hazards [6].

The techniques for the thermal management of rechargeable batteries have explored packaging [7], calorimetry [8, 9], external heating [10], local heating [11], heat flux measurement [12], over-reaction [13], respective irregularities [14], capacity decay [15], development of a machine learning method to estimate the state of health [16], discharge methodology [17], overcharge-analysis [18] and designing temperature resilient electrolytes [19].

Previous research works have analyzed thermal management in packing [20], design and adoption of heat-dissipating mini-channels [21], heat dissipation design [22], real time temperature monitoring [23] and heat treatment for the purpose of re-cycling [24].

Several works have investigated the variable heat dissipation rate due to unidirectional flow [25], non-invasive predicted the internal temperature from boundary conditions [26], and explored the radial variation in the thermal conductivity [27]. In a larger scale the heat pipes have been extensively utilized [28] and re-designed [29], where the transient heat-transfer has been predicted for high discharge rates [22]. Particularly, pulsating heat pipes (PHP), which possess high heat transfer efficiency, are utilized in electronics cooling and waste heat recovery [30]. Moreover the liquid cooling channels have been micro-architected in the pouch cell configuration [31] and analyzed versus channel size, inlet temperature, and inlet flow velocity [32]. As well, the utilization of phase change materials (PCM) has been explored as an efficient temperature control tool for safe operation in low-temperature range and is optimized versus the fin number and shape of the module [33].

Thus, new methods of development of batteries have been adapted, in terms of cost-effective geometrical designs, mainly due to the cost-effectiveness of a one-time installment. This has already been adapted and is trending in the electronic world, specifically in the coin cell, which has the possibility of scalability, particularly for stationary applications. New designs are proposed to optimize multiple factors, including component compatibility [34], primarily by requiring a minimal amount of material, considering the operational limitations. Furthermore, they excel in their reproducibility on large scales, simple bulk production, described by minimal dimensional conditions, generating its remarkable capability and simplicity in testing. However, the overheating and ignition at the vicinity of flash point temperature, remains a vital problem to overcome and optimize.

This paper tackles the most critical heat zone of the electrode-sealed sandwich cell battery, which is located at the central zone and carries the least heat dissipation. Therefore, a highly heat-conducting rod is devised, which absorbs the accumulated thermal energy and forks it out from the perpendicular

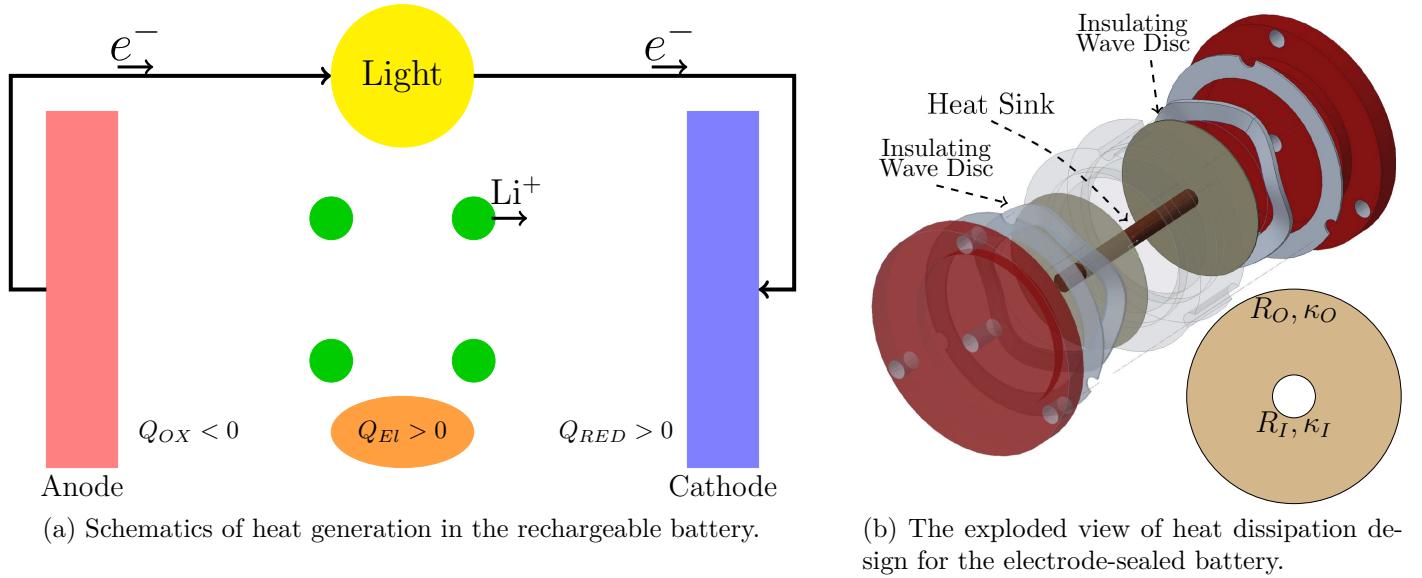


Figure 1: The heat generation and respective design for the central dissipation.

direction to the environment. Subsequently, the role of the material type and the relative scale of the heat sink is explored in the formation of the ultimate temperature profile, where the flash temperature of the electrolyte could be avoided. Moreover, attaining healthier heat management for the battery, opens the possibility of the use of low heat-diffusivity sustainable packaging materials, which are typically more recyclable and economical [35, 36].

2 Methodology

Figure 1a illustrates the ionic reaction and transport within the electrolyte. Although the oxidation and the reduction reactions are endothermic and exothermic with the same rate, neutralizing each other, the generated energy rate \dot{q}_{GEN} (i.e. heating up) is caused by the transport of the ions within the electrolytic medium. For the circular electrode if $T(r, t)$ represents the temperature at the radial distance r and the time t , therefore the temperature evolution is governed as [37]:

$$\frac{\partial T}{\partial t} = \alpha \left(\frac{\partial^2 T}{\partial r^2} + \frac{1}{r} \frac{\partial T}{\partial r} \right) + \frac{\dot{q}_{GEN}}{\rho c} \quad (1)$$

where r is the radial distance, that is confined between the inner and outer radii ($R_I \leq r \leq R_O$), α , ρ and c are the heat diffusivity, mass density and the specific heat capacity of the electrolyte. The rate of heat generation per unit volume \dot{q}_{GEN} is in fact the work of the drag force $F_d = 6\pi\mu av$ on the charge carriers with the radius a as [38]:

$$\dot{q}_{GEN} = \frac{F_d l}{Alt} N = \frac{6N\pi\mu a}{Al} v^2 \quad (2)$$

where l, t and v are the distance, the time and the velocity of ionic transfer in the inter-electrode space respectively, N is Avogadro's number and μ is the viscosity of the electrolyte. Having the current

relationship as $Q = iAt$ the Equation 2 is re-written as:

$$\dot{q}_{GEN} = 6\pi A\mu a Nl \left(\frac{i}{Q}\right)^2 \quad (3)$$

where i is the current density, A is the electrode area and Q is the amount of the transferred charge. The generated heat is typically transported to the boundaries and gets dissipated there. While such dissipation is more feasible for the boundary regions, mainly due to accessibility, it is the most difficult for the center to dissipate heat and as a result there is more heat accumulation in those regions. We could overcome with the temperature accumulation in the center by anticipating a heat-dissipating element as is illustrated in the Figure 1b. Such element could be a thin rod of certain conductivity, which is aligned in the perpendicular (in/out of plane) direction to the electrodes, providing the access to environment of the ambient temperature. Therefore, it could fork out the trapped heat locally from the central zone. While the respective thermal conductivity of the rod could vary, the metal choice would require the insulation from the electrode and current collectors in their connections by means of plastic sleeves. As well, the scale of the rod element could in fact be very small, compared to the rest of the battery, since the central region has relatively smaller area and generated heat.

Assuming the radii of the central element and the domain are R_I and R_O respectively, the boundary conditions will be the heat transfer rate in the inner and outer surfaces correlates with the respective temperature gradients (i.e. $\frac{\partial T}{\partial r}$) as well as the type of the medium (i.e. κ) for the heat transfer, as [39]:

$$\dot{q}_I = -\kappa_I \frac{\partial T}{\partial r} \Big|_{R_I}, \quad \dot{q}_O = -\kappa_O \frac{\partial T}{\partial r} \Big|_{R_O} \quad (4)$$

where \dot{q}_I , κ_I and \dot{q}_O , κ_O represent the heat dissipation rate and the thermal conductivity from the inner and outer surfaces respectively. The relationship 1 with the boundary conditions given in the equation 4 does not have a stable solution, since there is need for a constant value boundary condition. Therefore, solutions for the extreme cases of heat conductivity are assessed and divided into the inner-metallic ($\kappa_I \gg \kappa_O$) and outer-metallic ($\kappa_O \gg \kappa_I$) cases. The generated internal heat needs to pass through the electrolyte and the boundary material in series to dissipate to the environment. In this regard, a metallic boundary typically has orders of magnitude higher thermal conductivity than the electrolyte (i.e. $\kappa_{I,O} \gg \kappa_E$), which means that upon the generation of internal heat and initiation of the heat transfer, it passes the thermal energy through itself at a significantly faster rate than the electrolyte per se, leaving no internal energy inside. Technically this could be phrased as the material with extreme conductivity has thermally short-circuited with the environment, causing the metal to remain nearly at the same temperature as the ambient value. Hence the boundary condition could be expressed as:

$$\begin{cases} T_I \approx T_\infty & \text{Inner-metallic} \\ T_O \approx T_\infty & \text{Outer-metallic} \end{cases} \quad (5)$$

and these boundary conditions should be applied to the respective location of R_I and R_O as shown in the Figure 1b (bottom right).

Table 1: Physical / Computational Parameters.

Parameter	Value	Unit	Ref.	Parameter	Value	Unit	Ref.
μ_{EC}	2.64	<i>mpa.s</i>	[40]	R_I	1, 2, 5, 10	<i>mm</i>	Assumed
a	0.9	Å	[41, 42]	R_O	20	<i>mm</i>	Assumed
i	1	<i>mA.cm⁻²</i>	[43]	T_0	298	<i>K</i>	Standard
c	1750	<i>J.kg.K⁻¹</i>	[44]	$T_{g,EC}$	145	<i>°C</i>	[45] ¹
l	0.32	<i>cm</i>	[46, 47]	δr	150	<i>μm</i>	Assumed
κ_{EC}	0.21	<i>Wm⁻¹K⁻¹</i>	[48]	δt	6.2	<i>ms</i>	Equation 11
ρ_{EC}	1320	<i>kg.m⁻³</i>	[49]				

2.1 Ordinary Temperature Profile

From the temperature evolution relationship, given in the Equation 1, one can obtain the steady state profile by setting $\frac{\partial T}{\partial t} \approx 0$. In that case:

$$\frac{d}{dr} \left(r \frac{dT}{dr} \right) + \frac{\dot{q}_{GEN}}{\kappa_E} r = 0 \quad (6)$$

where $\kappa_E = \alpha \rho c$ is the thermal conductivity of the electrolyte. For the ordinary disk of radius R , the respective boundary conditions would be the ambient temperature in the outer boundary and the no variation of the temperature in the center due to symmetry, hence:

$$T_O = T_\infty, \quad \left. \frac{\partial T}{\partial r} \right|_{r=0} = 0 \quad (7)$$

Integrating the equation 6 twice one gets:

$$T = -\frac{\dot{q}_{GEN}}{4\kappa_E} r^2 + C_1 \ln(r) + C_2 \quad (8)$$

and applying the boundary conditions from the Equation 7 yields:

$$T(r) = \frac{\dot{q}_{GEN}}{4\kappa_E} (R^2 - r^2) + T_\infty \quad (9)$$

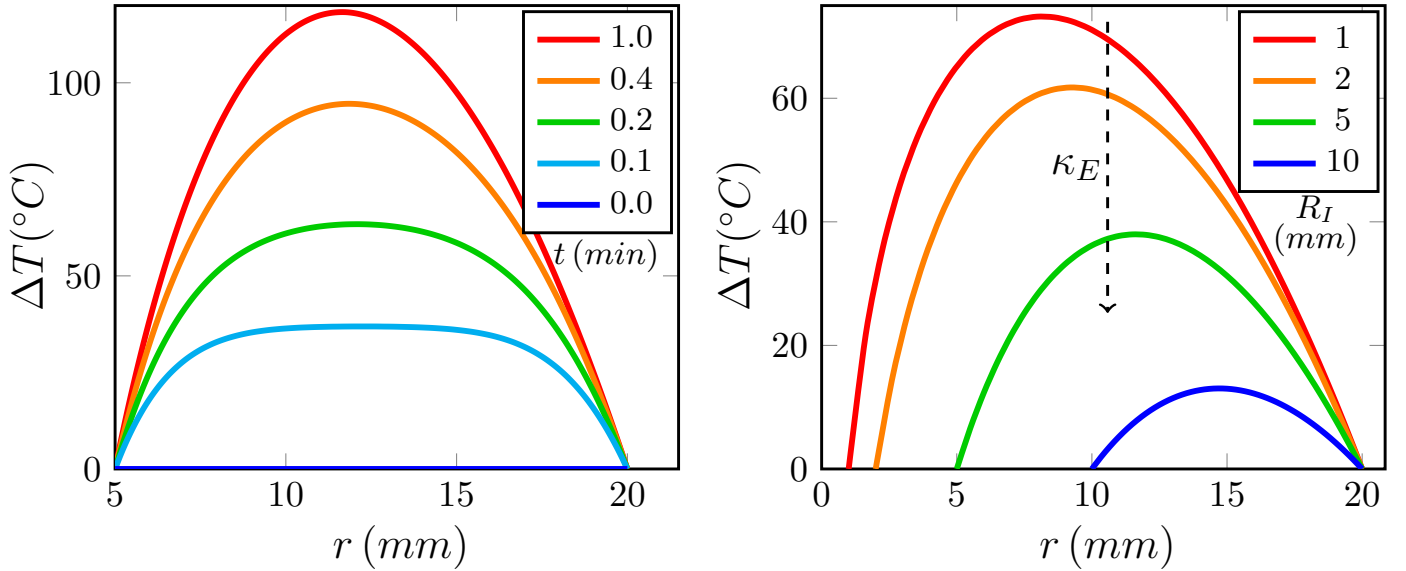
which shows a parabolic temperature distribution, with the maximum value in the center ($r = 0$) obtained as:

$$T_{max} = \frac{\dot{q}_{GEN}}{4\kappa_E} R^2 + T_\infty$$

2.2 Inner/Outer Metallic Boundary

The inclusion of the heat sink in the center could drastically reduce temperature values including the maximum temperature. In fact, if the temperature in the inner R_I and outer R_O boundaries is T_I and T_O respectively, the relationship 6 will have the following boundary conditions:

¹<https://pubchem.ncbi.nlm.nih.gov/compound/7303#section=Flash-Point>



(a) Transient Temperature Build-up ($\{R_I, R_O\} = \{0.5, 2\} m$) and $t = \{0.1, 0.2, 0.4, 1.0\} min$. (b) Steady-state Temperature profile (time-independent) with $R_I = \{1, 2, 5, 10\} mm$

Figure 2: The temperature profile versus time t , inner radius R_I and the electrolyte diffusivity α .

$$T_I = T_\infty, T_O = T_\infty \quad (10)$$

2.2.1 Transient Behavior

If T_i^j represents the temperature in the radial distance r_i and the time t^j , therefore the discretization of the relationship 1 is obtained as follows:

$$\frac{T_i^{j+1} - T_i^j}{\delta t} = \alpha \left(\frac{T_{i+1}^j - 2T_i^j + T_{i-1}^j}{\delta r^2} + \frac{1}{r_i} \frac{T_{i+1}^j - T_i^j}{\delta r} \right) + \frac{\dot{q}_{GEN}}{\rho c}$$

re-arranging gives:

$$T_i^{j+1} = \left(1 - \frac{2\alpha\delta t}{\delta r^2} - \frac{\alpha\delta t}{r_i\delta r} \right) T_i^j + \left(\frac{\alpha\delta t}{\delta r^2} + \frac{\alpha\delta t}{r_i\delta r} \right) T_{i+1}^j + \left(\frac{\alpha\delta t}{\delta r^2} \right) T_{i-1}^j + \frac{\dot{q}_{GEN}}{\rho c} \delta t$$

where, in order to have a stable solution, the resolution of the time intervals δt should be fine enough to capture the variation in the space, leading to a stable solution; hence, all the coefficients must be non-negative:

$$1 - \frac{2\alpha\delta t}{\delta r^2} - \frac{\alpha\delta t}{r_i\delta r} > 0$$

$$\delta t < \frac{1}{\frac{2\alpha}{\delta r^2} + \frac{\alpha}{r_i\delta r}}$$

In order to satisfy the above relationship since $\delta r \ll r_i$:

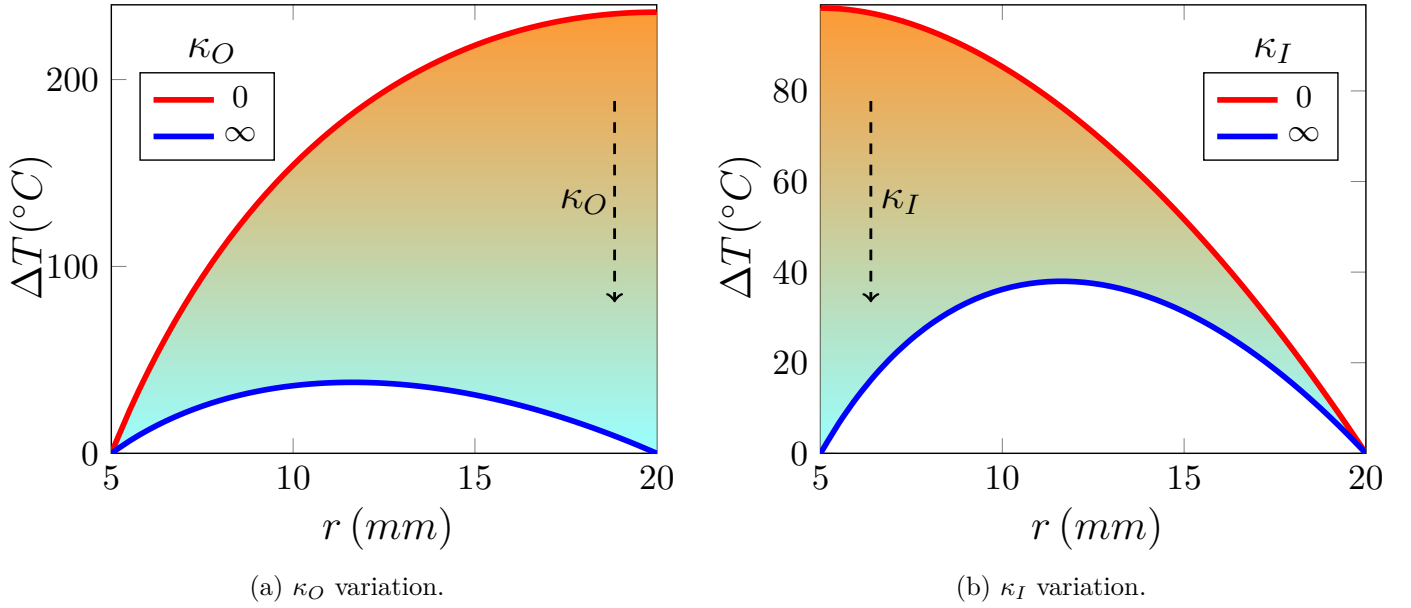


Figure 3: The steady-state temperature profile formed for all the ranges of inner κ_I and outer κ_O conductivities.

$$\frac{1}{3\alpha} < \frac{1}{\frac{2\alpha}{\delta r^2} + \frac{\alpha}{r_i \delta r}}$$

Therefore, the sufficient simplified resolution criterion would be:

$$\delta t \leq \frac{\delta r^2}{3\alpha} \quad (11)$$

The physical variables for calculating the temperature profiles are given in the Table 1. Additionally the heat diffusivity α , required for the stability criterion in the Equation 11, is calculated as [50]:

$$\alpha = \frac{\kappa}{\rho c} = \frac{0.21}{1320 \times 1750} = 9.1 \times 10^{-8} m^2.s^{-1}$$

Subsequently the transient temperature profile is computed using the stability criterion (Equation 11) which is illustrated in the Figure 2a for different times. Consequently, the temperature profile is investigated versus the scale of the inner sink in the Figure 2b. While the established temperature profiles are merely based on the realistic values from the battery components, they explore the role of their variation on the established temperature. As an example, Figure 2a shows the direction correlation of the temperature with the charging time in transient state ($t \uparrow \sim T \uparrow$) and the Figure 2b illustrates the inverse correlation of the temperature with the scale of the central heat dissipator ($R_I \uparrow \sim T \downarrow$).

2.2.2 Steady-state profile

For finding the steady-state temperature profile, double-integrating the equation 6 and imposing the boundary conditions from Equation 10, leads to:

$$\begin{cases} T_\infty = -\frac{\dot{q}_{GEN}}{4\kappa_E} R_I^2 + C_1 \ln(R_I) + C_2 \\ T_\infty = -\frac{\dot{q}_{GEN}}{4\kappa_E} R_O^2 + C_1 \ln(R_O) + C_2 \end{cases} \quad (12)$$

Replacing into the constant boundary conditions in equations 10 simplifies to:

$$\Delta T(r) = \frac{\dot{q}_{GEN}}{4\kappa_E} \left(\frac{(R_O^2 - R_I^2)}{\ln\left(\frac{R_O}{R_I}\right)} \ln\left(\frac{r}{R_I}\right) - (r^2 - R_I^2) \right) \quad (13)$$

where $\Delta T(r)$ is the rise in temperature with respect to ambient value ($\Delta T = T - T_\infty$).

2.3 Insulating Outer Medium

The insulating outer medium does not transfer the heat ($\kappa_O \rightarrow 0$), in this case the boundary condition changes to:

$$T_I = T_\infty, \quad \left. \frac{\partial T}{\partial r} \right|_{R_O} = 0 \quad (14)$$

Double-integrating the equation 6 and applying the above boundary conditions leads to:

$$\Delta T(r) = \frac{\dot{q}_{GEN}}{4\kappa_E} \left(R_O^2 \ln\left(\frac{r}{R_I}\right)^2 - (r^2 - R_I^2) \right) \quad (15)$$

2.4 Insulating Inner Medium

Regarding the insulating inner medium ($\kappa_I \rightarrow 0$), hence:

$$\left. \frac{\partial T}{\partial r} \right|_{R_I} = 0, \quad T_O = T_\infty \quad (16)$$

similarly double-integrating the equation 6 gives:

$$\Delta T(r) = \frac{\dot{q}_{GEN}}{4\kappa_E} \left(R_O^2 - r^2 + R_I^2 \ln\left(\frac{r}{R_O}\right)^2 \right) \quad (17)$$

The temperature profiles showing the extreme variations of the inner and outer media conductivity are provided in the Figures 3a and 3b respectively.

3 Experimental Setup

The experiments were performed using the manually-fabricated electrode-sealed sandwich cells (Figure 4), where the temperature measurements were taken in 3 distinct locations of center (T_I), mid-radius

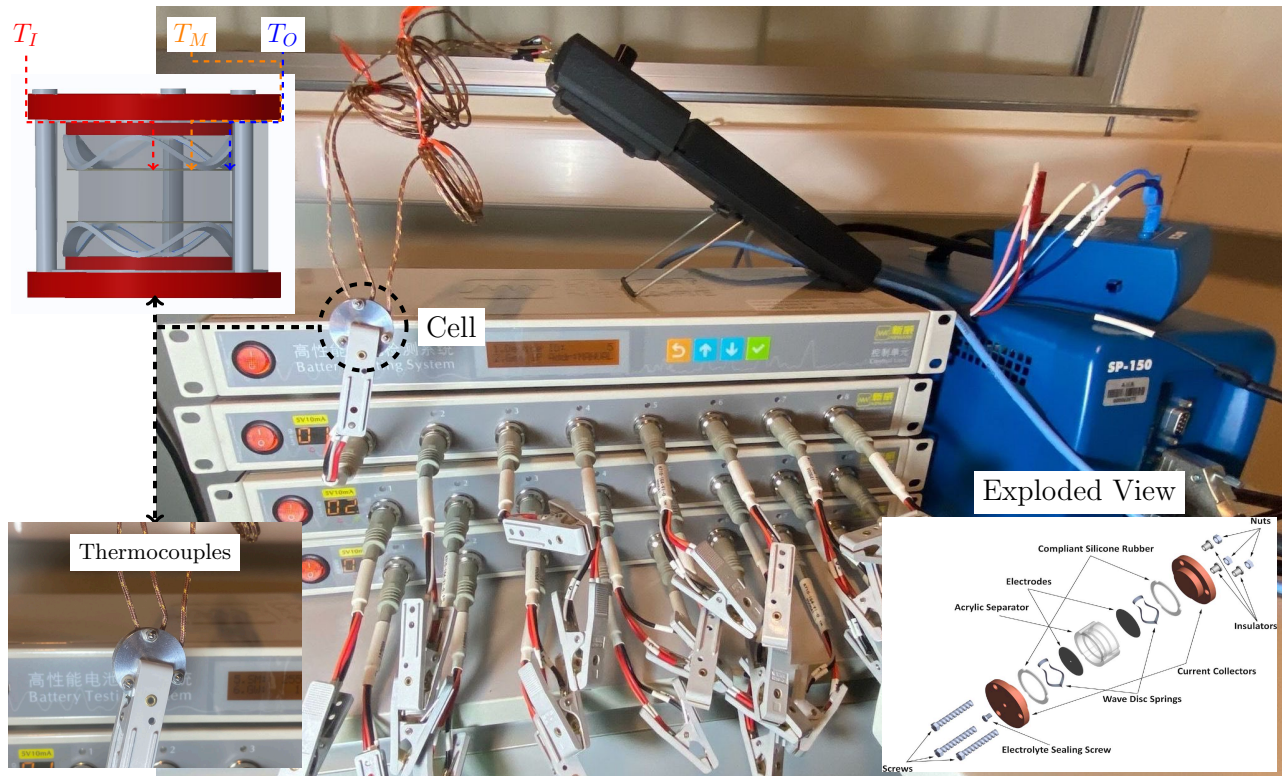


Figure 4: The experimental setup for the temperature measurements from the different zones of the cell. Top left: the placements of the thermocouple wires; Bottom left: zoom into the sandwich battery cell; Bottom right: exploded view of the cell components. [51].

(T_M) and outside (T_O) using thermocouples as illustrated in in the Figure 4 (top and bottom left). The sandwich cells consist of two circular electrodes, fabricated from lithium foil Li° as the anode and the lithium cobalt oxide $LiCoO_2$ as the cathode, which are separated by an electrolytic solution. The preparation was carried out as follows:

The lithium foil (Sigma Aldrich, 99.9%, 0.38mm thickness), was purchased and transferred to the argon-filled glovebox with controlled moisture and oxygen ($H_2O, O_2 < 1ppm$), manufactured by the Changshu Tongrun Electronic Co.Ltd. Subsequently, several electrodes with the diameter of the sandwich cell ($d = \frac{9}{16}$ ") were taken out via punching (purchased from McMaster-Carr) and were rinsed with the Dimethoxyethane (DME), which is the cleaning solvent. Moreover, the lithium cobalt oxide (Aldrich, 99.8% trace metals basis) was purchased and similarly prepared for utilization as the counter electrode. The screws, screw-insulators and nuts (shown in the Figure 4, bottom right), were purchased from McMaster-carr. The current-collectors were precision-machined from an Aluminum plate (purchased from McMaster-carr) to the matching dimensions with the screws and their insulators. As well, the separator housing was first purchased as a plate from McMaster-carr. Afterwards the laser-cut was used to extract circular rings from it. Finally, the machine mill was utilized to generate circular housing with an intermediate diameter, which matches with the diameters of the punched electrodes.

All the sandwich cell components were initially pre-assembled by placing on top of each other on the table and were fastened via the three screws on the periphery (Figure 4) [47]. The screws were protected by the plastic screw insulators as sleeves to avoid the electrical short circuit between the opposite current collectors. Furthermore, 3 thermocouple wires were inserted in during the pre-assembled status and were

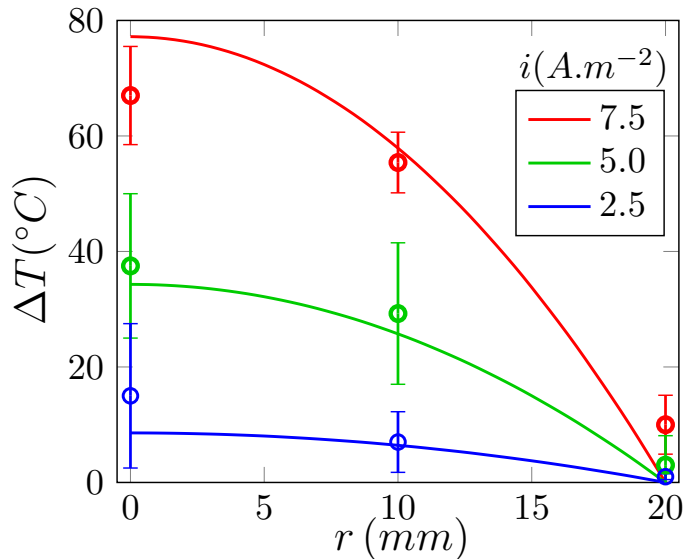


Figure 5: The steady-state temperature profiles, compared with the experimental values.

connected to the center, mid-radius and outside locations to track the local temperature values (Figure 4, top left and bottom left). Meanwhile, the wave discs were used in-between electrodes and their external packaging to create an insulating space, which gets filled with the gas from the glovebox (i.e. Argon) during the assembly. Such insulation ensures that the heat dissipation from electrode-side is negligible, albeit collecting the current by maintaining point connections between the electrodes and current collectors. The thermal insulation from the electrode-side is in fact the extreme case scenario for trapping the heat in batteries, where the dissipation from the boundary becomes the most emphasized.

The electrolyte solution was synthesized by mixing lithium hexafluorophosphate $LiPF_6$ (Aldrich, battery grade, $\geq 99.99\%$, trace metals basis) inside the ethylene carbonate EC (Aldrich, Anhydrous, 99%). Consequently, the electrolyte was injected via a syringe in the middle, which was closed and fastened by a wrapped teflon after.

Multiple cells were fabricated, were taken out of the glovebox and were cycled galvanostatically in the multi-channel Neware potentiostat ($5mA - 10V$) with the multitudes of current densities $\{0.25, 0.5, 0.75\} mA.cm^{-2}$ for 20 cycles. Throughout each experiment, the temperature value started to increase until reaching a steady-state temperature after passing through a transient state. Afterwards, the maximum temperature values were recorded, and their average and standard deviation were calculated, where for each point 3 separate experiments were carried out. Figure 5 visualizes and compares the obtained experimental values, versus the analytical temperature profile with similar parameters attained from Equation 6. The respective close correlations shows the consistency with our earlier formulation, where the central zone is the most critical.

4 Results & Discussions

The evolution of the temperature described in the Equation 1 is in fact the result of the competition of the generation (i.e. build-up) and the dissipation (i.e. loss) of the heat throughout the time, shown as below:

$$\left(\frac{\partial T}{\partial t}\right)_{TOT} = \left(\frac{\partial T}{\partial t}\right)_{GEN} + \left(\frac{\partial T}{\partial t}\right)_{DIS}$$

In fact, having the wholistic domain, one could break it down as the following:

$$\begin{cases} \left(\frac{\partial T}{\partial t}\right)_{GEN} = \frac{\dot{q}_{GEN}}{\rho c} \\ \left(\frac{\partial T}{\partial t}\right)_{DIS} = \alpha \left(\frac{\partial^2 T}{\partial r^2} + \frac{1}{r} \frac{\partial T}{\partial r} \right) \end{cases}$$

In fact the rate of heat generation remains constant by the current density, while the dissipation rate grows by the magnitude of the temperature and its gradient in the boundary with the ambient value, until both terms equalize finally in the steady state regime, as shown in the Figure 2a. More specifically, the slope and curvature of the temperature profile determines the dissipation rate, which is the highest in the steady-state regime. Such variations are visualized in the Figure 6 for an intermediate time (dashed) as well as steady-state condition (solid). While the generation term (*GEN*) favors the build-up of the temperature, the gradient of temperature between the inside and outside tends to increase the dissipation term (*DIS*) over time, mostly in the outer boundary, leading to the formation of the steady-state total temperature profile (*TOT*).

Additionally, the stability criterion given in the Equation 11 shows a finer segmentation of time versus space relative to the flat geometry with the typical resolution of $\delta t \leq \frac{\delta r^2}{2\alpha}$ [37]. This is due to higher sensitivity of variation in polar coordinates than the planar, since moving closer to the center squeezes the space to smaller segmentations with higher time precision.

The analytical relationship in the Equation 13 provides the possibility of locating the zone of maximum achievable temperature by setting $\left. \frac{\partial T}{\partial r} \right|_{r_{max}} = 0$ where:

$$\frac{dT}{dr} = -2r + \frac{(R_O^2 - R_I^2)}{\ln\left(\frac{R_O}{R_I}\right)} \frac{1}{r} = 0$$

and the location of maximum temperature r_{max} is obtained as:

$$r_{max} = \sqrt{\frac{R_O^2 - R_I^2}{2 \ln\left(\frac{R_O}{R_I}\right)}} \quad (18)$$

The maximum temperature rise ΔT_{max} is respectively attained as:

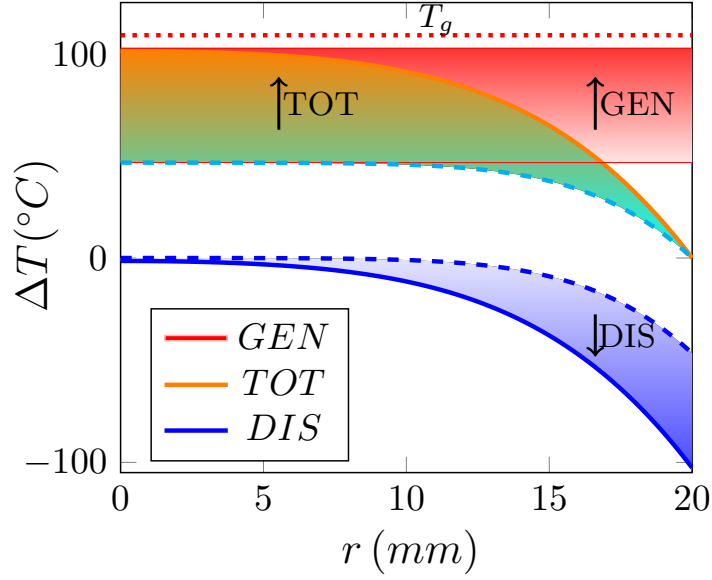


Figure 6: The competition between the profiles of heat generation (GEN) versus dissipation (DIS) terms, forming the resultant temperature profile (TOT). The arrows indicate the variation in time.

$$\Delta T_{max} = \frac{\dot{q}_{GEN}}{4\kappa_E} \left(R_I^2 + \frac{R_O^2 - R_I^2}{2 \ln \left(\frac{R_O}{R_I} \right)} \ln \left(\frac{R_O^2 - R_I^2}{R_I^2 \ln \left(\frac{R_O}{R_I} \right)^{2e}} \right) \right) \quad (19)$$

Herein we explore if the maximum temperature r_{max} falls within the inner half of the battery, which compared to the average radius r_{ave} and defining $\hat{R} := \frac{R_O}{R_I}$ yields:

$$\sqrt{\frac{\hat{R}^2 - 1}{2 \ln(\hat{R})}} < \frac{1}{2} (\hat{R} + 1) \quad (20)$$

simplifying leads to quadratic form as below:

$$\left(1 - \frac{\ln \hat{R}}{2} \right) \hat{R}^2 - (\ln \hat{R}) \cdot \hat{R} - 1 - \frac{\ln \hat{R}}{2} < 0 \quad (21)$$

herein, the 2 possibilities arise, based on the sign of the first coefficient:

I. $1 - \frac{\ln \hat{R}}{2} \leq 0$: since $\hat{R} > 0$, all the terms remain negative and the inequality is always true. Therefore:

$$\hat{R} \geq e^2 \quad (22)$$

II. For the case of $1 - \frac{\ln \hat{R}}{2} > 0$, the roots are found as:

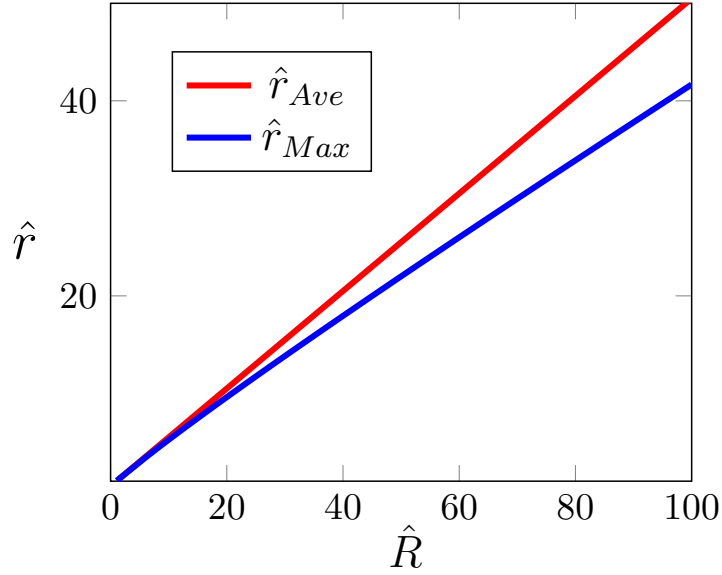


Figure 7: Comparison of \hat{r}_{Max} versus \hat{r}_{Ave} .

$$\Delta = (\ln \hat{R})^2 + 4 \left(1 - \left(\frac{\ln \hat{R}}{2} \right)^2 \right) = 4$$

$$\hat{R} = \frac{\ln \hat{R} \pm 2}{2 - \ln \hat{R}} = \begin{cases} \frac{2 + \ln \hat{R}}{2 - \ln \hat{R}} & \text{Larger} \\ -1 & \text{Smaller} \end{cases}$$

Since the quadratic equation is curving-up, the only case for negativity should fall between the roots:

$$-1 < \hat{R} \leq \frac{2 + \ln \hat{R}}{2 - \ln \hat{R}}$$

The left side of inequality is obvious, since $\hat{R} > 1$. Since in this case $1 < \hat{R} < e^2$, therefore $1 < \frac{2 + \ln \hat{R}}{2 - \ln \hat{R}} < \infty$. Therefore the *RHS* of the above inequality can get indefinitely larger and the inequality is already satisfied. Hence:

$$1 < \hat{R} < e^2 \quad (23)$$

From the Equations 22 and 23, since \hat{R} covers all the possible ranges, we have:

$$1 < \hat{R} < \infty \checkmark$$

and the equation 20 is always true for any given range of \hat{R} .

Thus, the maximum temperature always falls inside the inner half of the cell ($r_{max} < r_{ave}$). It is obvious from this Figure that the maximum location moves relatively further inside with respect to the scale ($\hat{r}_{Max}/\hat{r}_{Ave}$ reduces with the cell size). Moreover, while the maximum temperature T_{max} in the Equation 19 shows a non-linear relationship with the geometry (R_O, R_I and m), it is linearly proportional to the rate of heat generation \dot{q}_{GEN} and correlates inversely with the heat conductivity of

the electrolyte κ_E as:

$$\dot{q}_{GEN} \uparrow \sim T_{max} \uparrow, \kappa_E \uparrow \sim T_{max} \downarrow$$

Therefore, higher electrolyte heat conductivity κ_E (as well as higher heat diffusivity α , specific heat capacity c and density ρ , since $\kappa = \alpha\rho c$) leads to higher heat dissipation, forming a more alleviated temperature profile. On the other hand, it is physically obvious that the larger radius of the heat sink R_I provides higher dissipation and the maximum temperature gets reduced, as shown in the Figure 2b.

The percent error Err for the temperature correlation between the theoretical profile T_{THE} and experimental measurements T_{EXP} , which is visualized in the Figure 5, can be calculated as:

$$\text{Err} = \frac{1}{3} \sum_i \frac{|T_{THE,i} - T_{EXP,i}|}{T_{THE,i}}$$

and is obtained as $\{8.3\%, 4.9\%, 4.3\%\}$ for the current densities of $\{2.5, 5.0, 7.5\} A.m^{-2}$ respectively which is in the acceptable range. The possible error source for the higher theoretical number would be not considering the dissipation from the electrode side, or not considering the convection as another method of heat transfer. As well, the underlying reason for the lower theoretical temperature could be the limited experimental thermal conductivity in the boundary, which causes more temperature build-up with respect to the modeling.

Finally, it is obvious the maximum temperature T_{max} is highest when the boundaries become insulating (Figures 3a and 3b). Such difference particularly is the highest for the outer-insulating medium and the underlying reason would be the higher surface area for heat dissipation than the inner boundary ($R_O > R_I$).

Needless to mention that if the assembled battery was not sealed, the heat dissipation would additionally occur from the electrodes surface as well, where two additional boundary conditions occur as follows:

$$\dot{q}_{Bot} = -\kappa_{Bot} \frac{\partial T}{\partial y} \Big|_{y=0}, \dot{q}_{Top} = -\kappa_{Top} \frac{\partial T}{\partial y} \Big|_{y=l} \quad (24)$$

where y is the variable for the vertical distance and $\dot{q}_{Bot}, \dot{q}_{Top}$ and $\kappa_{Bot}, \kappa_{Top}$ are the rate of heat dissipation and heat conductivities of the top and bottom boundaries respectively.

5 Conclusions

In this paper a new design was proposed for the effective heat dissipation from the most critical zone (i.e. center) of the electrode-sealed batteries and was analyzed versus the physical (i.e. thermal conductivity) and geometrical (i.e. scale) properties. After the initial calculation of the transient evolution of the temperature distribution, the steady state profile was analytically obtained. In the next step, the original experiments were performed on the manually-fabricated sealed sandwich batteries which formed substantially high temperature in the central zone. Subsequently, a central metallic heat sink was

implemented, which forks out the heat from in/out plane directions, and the respective location and the drop of the (maximum) temperature was quantified. It was analytically proven that for any scale of the heat-dissipating element the maximum temperature falls closer to the center than the periphery of the cell, which relatively moves further inside with the scale. Furthermore, it is illustrated that due to the curved boundaries a lower resolution of time-to-space ($\approx 33\%$) is required relative to the flat surfaces for capturing the transient temperature evolution. Finally, it was deciphered that the temperature build-up is in terms of the competitive elements of heat generation from the current density and dissipation due to temperature gradient from the boundaries. The obtained extremums and the respective analysis can be used for effective design of performance measures for the temperature control during the charging period of the batteries, particularly for those involved in packed clusters or fabricated with recyclable packaging, where the heat has the least possibility to escape.

Acknowledgment

The authors would like to thank the support from Masri Institute at American University of Beirut, Grant Award No. 103919 for the Research Assistant Fadi Elias.

List of Symbols

l : inter-electrode distance (m)	R_I : inner radius of of cell (m)
\dot{q}_{GEN} : rate of heat generation per area ($J.m^{-2}.s^{-1}$)	R_O : outer radius of of cell (m)
N : Avogadro's number ($6 \times 10^{23} atoms.mol^{-1}$)	μ : viscosity of $LiPF_6$ ($mpa.s$)
T_∞ : ambient temperature (K)	a : ionic radius of Li^+ (\AA)
κ_I : inner thermal conductivity ($W.m^{-1}.K^{-1}$)	i : current density ($A.m^{-2}$)
κ_O : outer thermal conductivity ($W.m^{-1}.K^{-1}$)	A : electrode area (m^2)
κ_E : electrolyte thermal conductivity ($W.m^{-1}.K^{-1}$)	Q : amount of charge (C)
ρ : electrolyte density ($kg.m^{-3}$)	α : thermal diffusivity ($m^2.s^{-1}$)
t : time (s)	T : absolute temperature (K)
v : velocity of ionic transfer ($m.s^{-1}$)	r : radial spatial coordinate (m)
F_d : Drag force on the charge carriers (N)	c : specific heat ($J.kg.K^{-1}$)
δr : radial segmentation (m)	T_g : flash point (K)
δt : time segmentation (s)	ΔT : temperature rise ($T - T_\infty$)

Data Availability

The row data for producing the results in this manuscript are freely available upon request from the corresponding author at aryanfar@caltech.edu.

Conflict of Interest Statement

The authors declare that they have no competing financial interests to influence the work reported in this paper.

References

- [1] John Shalf. The future of computing beyond moores law. *Philosophical Transactions of the Royal Society A*, 378(2166):20190061, 2020.
- [2] Jeff Tollefson. Charging up the future: a new generation of lithium-ion batteries, coupled with rising oil prices and the need to address climate change, has sparked a global race to electrify transportation. *Nature*, 456(7221):436–441, 2008.
- [3] Dwayne N Fry, David E Holcomb, John K Munro, Lester C Oakes, and MJ Matson. Compact portable electric power sources. Technical report, Oak Ridge National Lab.(ORNL), Oak Ridge, TN (United States), 1997.
- [4] George Crabtree, Elizabeth Kócs, and Lynn Trahey. The energy-storage frontier: Lithium-ion batteries and beyond. *Mrs Bulletin*, 40(12):1067–1078, 2015.
- [5] Peter J Hall and Euan J Bain. Energy-storage technologies and electricity generation. *Energy policy*, 36(12):4352–4355, 2008.
- [6] Dongxu Ouyang, Mingyi Chen, Que Huang, Jingwen Weng, Zhi Wang, and Jian Wang. A review on the thermal hazards of the lithium-ion battery and the corresponding countermeasures. *Applied Sciences*, 9(12):2483, 2019.
- [7] XM Xu and R He. Review on the heat dissipation performance of battery pack with different structures and operation conditions. *Renewable and sustainable energy reviews*, 29:301–315, 2014.
- [8] Xuan Liu, Stanislav I Stoliarov, Matthew Denlinger, Alvaro Masias, and Kent Snyder. Comprehensive calorimetry of the thermally-induced failure of a lithium ion battery. *Journal of Power Sources*, 280:516–525, 2015.
- [9] Yangyang Fu, Song Lu, Kaiyuan Li, Changchen Liu, Xudong Cheng, and Heping Zhang. An experimental study on burning behaviors of 18650 lithium ion batteries using a cone calorimeter. *Journal of Power Sources*, 273:216–222, 2015.
- [10] Changyong Jin, Yuedong Sun, Huaibin Wang, Xin Lai, Shuyu Wang, Siqu Chen, Xinyu Rui, Yuejiu Zheng, Xuning Feng, Hewu Wang, et al. Model and experiments to investigate thermal runaway characterization of lithium-ion batteries induced by external heating method. *Journal of Power Sources*, 504:230065, 2021.

- [11] Zhao Lei, Zhu Maotao, Xu Xiaoming, and Gao Junkui. Thermal runaway characteristics on ncm lithium-ion batteries triggered by local heating under different heat dissipation conditions. *Applied Thermal Engineering*, 159:113847, 2019.
- [12] Chen Liang, Lihua Jiang, Shuliang Ye, Zhaoyu Wang, Zesen Wei, Qingsong Wang, and Jinhua Sun. Precise in-situ and ex-situ study on thermal behavior of lini1/3co1/3mn1/3o2/graphite coin cell: From part to the whole cell. *Journal of Energy Chemistry*, 54:332–341, 2021.
- [13] Randolph A Leising, Marcus J Palazzo, Esther Sans Takeuchi, and Kenneth J Takeuchi. A study of the overcharge reaction of lithium-ion batteries. *Journal of power sources*, 97:681–683, 2001.
- [14] Fiona C Strobridge, Bernardo Orvananos, Mark Croft, Hui-Chia Yu, Rosa Robert, Hao Liu, Zhong Zhong, Thomas Connolley, Michael Drakopoulos, Katsuyo Thornton, et al. Mapping the inhomogeneous electrochemical reaction through porous lifepo4-electrodes in a standard coin cell battery. *Chemistry of Materials*, 27(7):2374–2386, 2015.
- [15] Sung Park, Andreas Savvides, and Mani B Srivastava. Battery capacity measurement and analysis using lithium coin cell battery. In *ISLPED'01: Proceedings of the 2001 International Symposium on Low Power Electronics and Design (IEEE Cat. No. 01TH8581)*, pages 382–387. IEEE, 2001.
- [16] Jianyu Zhang and Wei Lu. Sparse data machine learning for battery health estimation and optimal design incorporating material characteristics. *Applied Energy*, 307:118165, 2022.
- [17] Yin Zhang and John N Harb. Performance characteristics of lithium coin cells for use in wireless sensing systems: Transient behavior during pulse discharge. *Journal of power sources*, 229:299–307, 2013.
- [18] Chen Liang, Lihua Jiang, Shuliang Ye, Jinhua Sun, and Qingsong Wang. Comprehensive analysis on dynamic heat generation of lini1/3co1/3mn1/3o2 coin cell under overcharge. *Journal of The Electrochemical Society*, 166(14):A3369, 2019.
- [19] Marco-Tulio F Rodrigues, Kaushik Kalaga, Hemtej Gullapalli, Ganguli Babu, Arava Leela Mohana Reddy, and Pulickel M Ajayan. Hexagonal boron nitride-based electrolyte composite for li-ion battery operation from room temperature to 150Å° c. *Advanced Energy Materials*, 6(12):1600218, 2016.
- [20] H Fayaz, Asif Afzal, AD Samee, Manzoore Elahi M Soudagar, Naveed Akram, MA Mujtaba, RD Jilte, Md Islam, Ümit Ağbulut, C Ahamed Saleel, et al. Optimization of thermal and structural design in lithium-ion batteries to obtain energy efficient battery thermal management system (btms): a critical review. *Archives of Computational Methods in Engineering*, pages 1–66, 2021.
- [21] Wei Li, Xiongbin Peng, Mi Xiao, Akhil Garg, and Liang Gao. Multi-objective design optimization for mini-channel cooling battery thermal management system in an electric vehicle. *International Journal of Energy Research*, 43(8):3668–3680, 2019.

- [22] Mao-Sung Wu, KH Liu, Yung-Yun Wang, and Chi-Chao Wan. Heat dissipation design for lithium-ion batteries. *Journal of power sources*, 109(1):160–166, 2002.
- [23] Panding Wang, Xinyi Zhang, Le Yang, Xingyu Zhang, Meng Yang, Haosen Chen, and Daining Fang. Real-time monitoring of internal temperature evolution of the lithium-ion coin cell battery during the charge and discharge process. *Extreme Mechanics Letters*, 9:459–466, 2016.
- [24] Yue Yang, Emenike G Okonkwo, Guoyong Huang, Shengming Xu, Wei Sun, and Yinghe He. On the sustainability of lithium ion battery industry—a review and perspective. *Energy Storage Materials*, 36:186–212, 2021.
- [25] D Sarkar, K Shah, A Haji-Sheikh, and A Jain. Analytical modeling of temperature distribution in an anisotropic cylinder with circumferentially-varying convective heat transfer. *International Journal of Heat and Mass Transfer*, 79:1027–1033, 2014.
- [26] Dean Anthony, Daipayan Sarkar, and Ankur Jain. Non-invasive, transient determination of the core temperature of a heat-generating solid body. *Scientific Reports*, 6(1):1–10, 2016.
- [27] Long Zhou, Mohammad Parhizi, and Ankur Jain. Temperature distribution in a multi-layer cylinder with circumferentially-varying convective heat transfer boundary conditions, 2021.
- [28] Marco Bernagozzi, Anastasios Georgoulas, Nicolas Miche, and Marco Marengo. Heat pipes in battery thermal management systems for electric vehicles: A critical review. *Applied Thermal Engineering*, page 119495, 2022.
- [29] Yueqi Wang, Dan Dan, Yangjun Zhang, Yuping Qian, Satyam Panchal, Michael Fowler, Weifeng Li, Manh-Kien Tran, and Yi Xie. A novel heat dissipation structure based on flat heat pipe for battery thermal management system. *International Journal of Energy Research*, 46(11):15961–15980, 2022.
- [30] Xiaohong Han, Xuehui Wang, Haoce Zheng, Xiangguo Xu, and Guangming Chen. Review of the development of pulsating heat pipe for heat dissipation. *Renewable and Sustainable Energy Reviews*, 59:692–709, 2016.
- [31] Mahesh Suresh Patil, Jae-Hyeong Seo, Satyam Panchal, and Moo-Yeon Lee. Numerical study on sensitivity analysis of factors influencing liquid cooling with double cold-plate for lithium-ion pouch cell. *International Journal of Energy Research*, 45(2):2533–2559, 2021.
- [32] Jiabin Duan, Jiapei Zhao, Xinke Li, Satyam Panchal, Jinliang Yuan, Roydon Fraser, and Michael Fowler. Modeling and analysis of heat dissipation for liquid cooling lithium-ion batteries. *Energies*, 14(14):4187, 2021.
- [33] VG Choudhari, AS Dhoble, and Satyam Panchal. Numerical analysis of different fin structures in phase change material module for battery thermal management system and its optimization. *International Journal of Heat and Mass Transfer*, 163:120434, 2020.

- [34] Patrick Bonnick and JR Dahn. A simple coin cell design for testing rechargeable zinc-air or alkaline battery systems. *Journal of The Electrochemical Society*, 159(7):A981, 2012.
- [35] Naoki Nitta, Feixiang Wu, Jung Tae Lee, and Gleb Yushin. Li-ion battery materials: present and future. *Materials today*, 18(5):252–264, 2015.
- [36] Fereshteh Samimi, Aziz Babapoor, Mohammadmehdi Azizi, and Gholamreza Karimi. Thermal management analysis of a li-ion battery cell using phase change material loaded with carbon fibers. *Energy*, 96:355–371, 2016.
- [37] Theodore L Bergman, Theodore L Bergman, Frank P Incropera, David P Dewitt, and Adrienne S Lavine. *Fundamentals of heat and mass transfer*. John Wiley & Sons, 2011.
- [38] Robert W Fox, Alan T McDonald, and John W Mitchell. *Fox and McDonald’s introduction to fluid mechanics*. John Wiley & Sons, 2020.
- [39] Yaman Yener and Sadık Kakaç. *Heat conduction*. CRC Press, 2018.
- [40] ER Logan, Erin M Tonita, KL Gering, Lin Ma, Michael KG Bauer, Jing Li, LY Beaulieu, and JR Dahn. A study of the transport properties of ethylene carbonate-free li electrolytes. *Journal of The Electrochemical Society*, 165(3):A705, 2018.
- [41] Asghar Aryanfar, Sajed Medlej, and William A Goddard III. Morphometry of dendritic materials in rechargeable batteries. *Journal of Power Sources*, 481:228914, 2021.
- [42] Robert D Shannon. Revised effective ionic radii and systematic studies of interatomic distances in halides and chalcogenides. *Acta crystallographica section A: crystal physics, diffraction, theoretical and general crystallography*, 32(5):751–767, 1976.
- [43] F. Orsini A.D. Pasquier B. Beaudoin J.M. Tarascon. In situ scanning electron microscopy (sem) observation of interfaces with plastic lithium batteries. *J. Power Sources*, 76:19–29, 1998.
- [44] NIST NIST. Reference on constants, units and uncertainty.
- [45] Steffen Hess, Margret Wohlfahrt-Mehrens, and Mario Wachtler. Flammability of li-ion battery electrolytes: flash point and self-extinguishing time measurements. *Journal of The Electrochemical Society*, 162(2):A3084, 2015.
- [46] SR Narayanan, S Surampudi, AI Attia, and CP Bankston. Analysis of redox additive-based overcharge protection for rechargeable lithium batteries. *Journal of the electrochemical Society*, 138(8):2224, 1991.
- [47] Asghar Aryanfar, Daniel Brooks, Boris V. Merinov, William A. Goddard Iii, AgustĂn J. Colussi, and Michael R. Hoffmann. Dynamics of lithium dendrite growth and inhibition: Pulse charging experiments and monte carlo calculations. *The Journal of Physical Chemistry Letters*, 5(10):1721–1726, 2014.

- [48] Paul H Johnson. The properties of ethylene carbonate and its use in electrochemical applications a literature review. 1985.
- [49] William M Haynes. *CRC handbook of chemistry and physics*. CRC press, 2014.
- [50] R Byron Bird. Transport phenomena. *Appl. Mech. Rev.*, 55(1):R1–R4, 2002.
- [51] Asghar Aryanfar. Method and device for dendrite research and discovery in batteries, April 11 2017. US Patent 9,620,808.